

Zhuang, L., Jung, S. G., Diaz, M., Kim, K. Y., Hofmann, H., Min, K.-B., Zang, A., Stephansson, O., Zimmermann, G., Yoon, J.-S. (2020): Laboratory True Triaxial Hydraulic Fracturing of Granite Under Six Fluid Injection Schemes and Grain-Scale Fracture Observations. - Rock Mechanics and Rock Engineering, 53, 4329-4344.

<https://doi.org/10.1007/s00603-020-02170-8>

Laboratory True Triaxial Hydraulic Fracturing of Granite Under Six Fluid Injection Schemes and Grain-Scale Fracture Observations

Li Zhuang¹ · Sung Gyu Jung² · Melvin Diaz³ · Kwang Yeom Kim³ · Hannes Hofmann⁴ · Ki-Bok Min⁵ · Arno Zang⁴ · Ove Stephansson⁴ · Günter Zimmermann⁴ · Jeoung-Seok Yoon⁶

Abstract

Laboratory hydraulic fracturing tests on cubic granite specimens with a side length of 100 mm were performed under true triaxial stress conditions combined with acoustic emission monitoring. Six different injection schemes were applied to investigate the influence of the injection scheme on hydraulic performance and induced seismicity during hydraulic fracturing. Three of these schemes are injection rate controlled: constant rate continuous injection (CCI), stepwise rate continuous injection (SCI), and cyclic progressive injection (CPI); the other three are pressurization rate controlled: stepwise pressurization (SP), stepwise pulse pressurization (SPP) and cyclic pulse pressurization (CPP). The test results show that the SPP scheme achieves the highest increase in injectivity among the six schemes. The CPI scheme generates the lowest induced seismicity while the improvement in injectivity is the least pronounced. The CPP scheme allows increasing injectivity and decreasing induced seismicity, and is suggested as a promising alternative injection scheme for field applications. Thin section microscopic observations of fractured specimens show that intragranular fractures splitting microcline, orthoclase and quartz grains dominate the hydraulic fractures independent of the injection scheme. The SPP scheme creates the largest fracture length, which explains the highest injectivity value among all schemes. Tests with relatively low magnitude of maximum AE amplitude correspond to short fracture length and small portions of intragranular fractures in microcline grains. Quartz grains are more fractured than microcline and orthoclase grains, and quartz chips (natural proppants) are frequently observed adjacent to hydraulic fractures. The laboratory test results show the potential for hydraulic fracture growth control in field applications by advanced fluid injection schemes, i.e. cyclic pulse pressurization of granitic rock mass.

Keywords Injection scheme · Cyclic hydraulic fracturing · Pulse pressurization · Injectivity · Induced seismicity · Thin section microscopy

1 Introduction

Hydraulic fracturing in crystalline rock has become increasingly important in geothermal development, especially for enhanced geothermal system (EGS). However, induced or triggered earthquakes reported from EGS sites is one of the main technical hurdles encountered (Majer et al. 2007; McGarr 2014; Grigoli et al. 2018). A number of new alternative stimulation strategies have been introduced to prevent larger magnitudes of induced seismicity (Zang et al. 2013, 2019; Meier et al. 2015) and a preliminary field demonstration of cyclic soft stimulation concept was implemented (Hofmann et al. 2018a, 2019). At laboratory scale, cyclic hydraulic fracturing (CHF), compared to conventional hydraulic fracturing (HF) with continuous injection, has been shown to reduce the breakdown pressure (BP) for granitic rocks and the

✉ Li Zhuang
zhuangli@kict.re.kr

✉ Kwang Yeom Kim
kykim@kmou.ac.kr

¹ Korea Institute of Civil Engineering and Building Technology, Goyang 10223, Korea

² University of Science and Technology, Daejeon 34113, Korea

³ Korea Maritime and Ocean University (formerly at Korea Institute of Civil Engineering and Building Technology), Busan 49112, Korea

⁴ Helmholtz Centre Potsdam GFZ German Research Centre for Geosciences, 14473 Potsdam, Germany

⁵ Department of Energy Resources Engineering and Research Institute of Energy and Resources, Seoul National University, Seoul 08826, Republic of Korea

⁶ DynaFrax UG, 14467 Potsdam, Germany

maximum amplitude of induced seismicity (Zhuang et al. 2018a, b, 2019b; Diaz et al. 2018a, b, c; Stephansson et al. 2019) and at mine scale in the Äspö Hard Rock Laboratory (HRL) (Zang et al. 2017, 2019; Hofmann et al. 2018a; Zimmermann et al. 2019). However, the permeability enhancement effect caused by CHF was less pronounced on either the laboratory or mine scale (Zhuang et al. 2019b; Zimmermann et al. 2019). A conflicting result showing that CHF increases fracture permeability more than conventional HF has been reported by Patel et al. (2017) for Tennessee sandstone. Zhou et al. (2017, 2018) tested CHF in concrete samples, demonstrating that CHF could help generate fractures of greater complexity and lead to better permeability enhancement than that achieved by conventional HF. These contrasting observations are attributed to different rock types. Past studies have shown that HF behavior differs for igneous rocks, sedimentary rocks (Stanchits et al. 2012; Patel et al. 2017) and rock-like materials such as gypsum and cement (Haimson and Fairhurst 1969; Guo et al. 1993; Zhou et al. 2017, 2018). Even for the same classification of granitic rocks, HF is influenced by grain size (Ishida et al. 2000), mineral composition and internal flaws (Stephansson et al. 2019).

For HF in granitic rocks or sandstones, permeability enhancement and induced seismicity are highly related to the injection scheme (Zimmermann et al. 2010; Zang et al. 2019; Hofmann et al. 2018b). Zang et al. (2013, 2019) proposed fatigue hydraulic fracturing (FHF) treatment, which is a combination of modified CHF and pulse pressurization. Experimental results of granitic rocks in the Äspö HRL show that best permeability performance at mine scale was obtained by FHF, and is five times the permeability obtained by the conventional HF (Zang et al. 2017; Zimmermann et al. 2019). They infer that high-frequency water pulses disintegrate and remove weak material from the walls of the fracture by hydraulic fatigue and locally decrease the strength of rock by generating an enlarged fracture damage zone (Zang et al. 2019).

Pulse hydraulic fracturing (PHF) is a typical stimulation method with dynamic loading. The concept of PHF and its modified method were introduced decades ago and have been applied

for reservoir stimulation to improve productivity (Hunt and Shu 1989). PHF was also frequently used for coalbed methane exploitation because methane gas is usually stored in relatively low permeability reservoirs (Li et al. 2014; Wu et al. 2016; Xu et al. 2017). However, the use of PHF in hard rock formations was rarely reported while pulsed water jet was applied for breaking hard rocks (Dehkhoda and Hood 2013). Recently, Stephansson et al. (2019) investigated the PHF behavior of three different granitic sample cores obtained from the Äspö HRL mine scale test borehole and surmised that the reduction in breakdown pressure from cyclic pressurization and dynamic pulsing is dependent on rock type. In their study, effect of various fluid injection schemes has not been compared and investigated.

In this study, we investigate the influence of injection schemes on injection-induced seismicity and permeability enhancement. For this, we selected six different injection schemes including both continuous injection and cyclic injections and their modified injection patterns (cyclic and pulse pressurization) for laboratory experiments. PHF was included to investigate its effect on granite and the mechanism behind it. This paper mainly presents data of the hydraulic performance after fracturing and observations of hydraulic fractures.

2 Experimental setup

2.1 True Triaxial Hydraulic Fracturing Test Equipment

A true triaxial hydraulic fracturing test setup (Fig. 1) was used for the experiments (Zhuang et al. 2018a). The maximum applied stress for the cubic block with side length of 100 mm is 10 MPa, and the maximum injection pressure provided by the servo-control hydraulic pump is 35 MPa. Fluid can be injected under a controlled pressurization rate, or injection rate, or a combination of the two. The pressurization can be applied in various ways, including linear and periodic functions, among others.

2.2 Test Specimens, Stress Conditions, And Acoustic Emission Monitoring

Cubic specimens of Pocheon granite with a side length of 100 mm and with a 5-mm diameter,

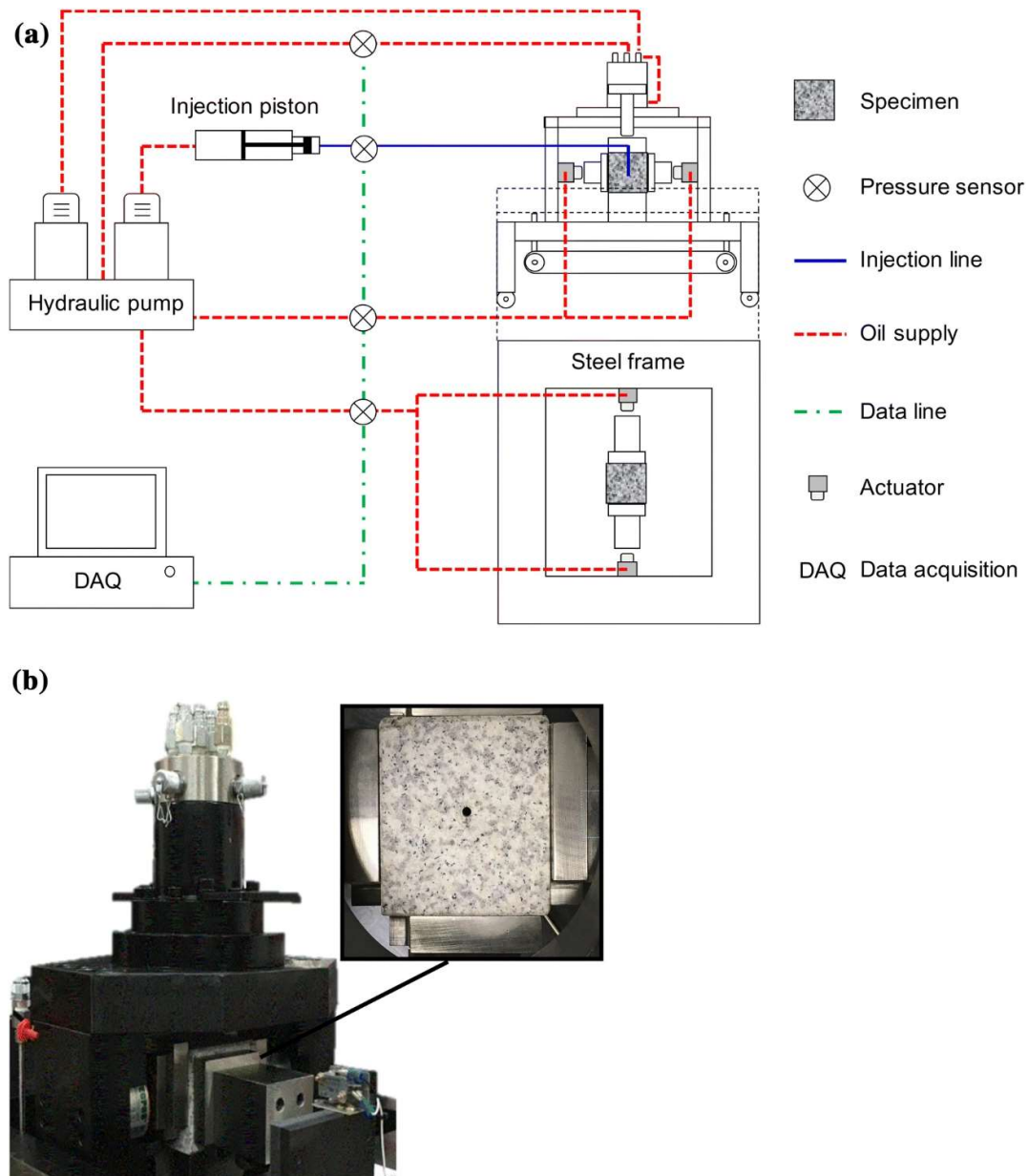


Figure 1. True triaxial hydraulic fracturing test system: **a** Schematic diagram; **b** photograph of the main part and sample installation (hydraulic pump was not included)

and 70 mm deep borehole at the top of the specimen is used for testing, as shown in Fig. 2. We selected a borehole depth larger than the half of sample height, expecting a larger rock volume available for fracture propagation because the fracture usually propagates upwards. The granite has a measured effective porosity of 0.66% and permeability of ~ 0.01 mD. A few important average anisotropic physical and mechanical properties of Pocheon granite at both dry and saturated conditions are given in Table 1. For detailed information about testing method and data analysis we refer to Zhuang et al. (2019a,

2020). The granite has strong anisotropy compared to other granitic rocks. The anisotropy of granites with microscopic fabric is analyzed according to Douglass and Voight (1969). The three cleavage planes, called rift, grain and hardway, cannot be ignored in laboratory scale testing on either mechanical or hydraulic fracturing (Zhuang et al. 2016, 2019a, 2020). The applied three principal stresses are 4 MPa in vertical direction, 6 MPa for the maximum horizontal stress and 3 MPa for the minimum horizontal stress. The maximum horizontal stress is applied perpendicular to the hardway plane;

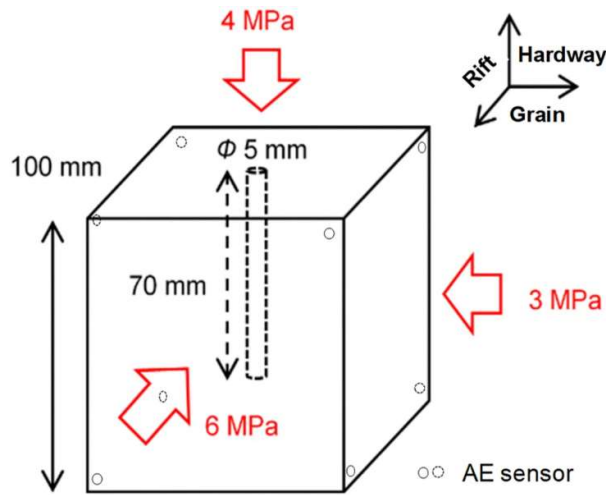


Figure 2. Sketch of granite cubic specimen and applied stress conditions. The maximum horizontal stress is parallel to the rift plane, which has the lowest tensile strength among the three cleavages

therefore, fractures are expected to be generated along the rift plane, which has the smallest tensile strength and mode I fracture toughness among the three cleavage planes (Zhuang et al. 2016, 2020).

Acoustic emission monitoring was applied during the experiments, and eight Nano30 sensors were directly installed on the corners of the specimens (Fig. 1b), which are blind zones for external pressure. Two sensors were attached at corners of each lateral face of the sample, and none on the top and bottom. A high-vacuum grease coupling agent enhances the contact between the sensors and rock surface. AE signals were amplified using a 40-dB preamplifier. After testing the background noise and the threshold amplitudes were set to 40–52 dB for different cases. Later, the AE monitoring results were

filtered based on the same upper limit of 52 dB. AE data were acquired using the AEwin software (MISTRAS group Inc. 2014).

2.3 Injection Scheme

Six different injection schemes used in this study are shown in Fig. 3. The first three are injection rate controlled and the last three are pressurization rate controlled. These injection schemes were selected based on recent experimental findings that cyclic injection has the advantage to lower magnitudes of seismic events, while hydraulic performance improvement is less compared to that of continuous injection (Zimmermann et al. 2019; Zhuang et al. 2019b), and pulse pressurization contributes to permeability enhancement (Zang et al. 2019). Figure 3a, b shows continuous injection with constant rate (CCI) and stepwise rate (SCI) increase, respectively. Figure 3c shows cyclic progressive injection (CPI) where in each cycle high and low injection rates alternate and the high injection rates increase with the increasing number of cycles. The maximum injection rate was limited to 100 mm³/s in the SCI and CPI injection schemes for comparison with the CCI scheme at the same constant injection rate. Figure 3d shows the stepwise pressurization (SP) scheme, where the injection pressure was increased under a constant pressurization rate by multiple stages. This scheme is designed as a comparison for schemes with pulse pressurization, as the equipment only allows dynamic pulsing to be applied under pressurization rate control. Figure 3e is a modification of the SP scheme with each stage ending with pulse pressurization.

Table 1

Average measurements of physical and mechanical parameters of three planes of cleavage for Pocheon granite in laboratory

Plane of cleavage	Hydraulic conductivity (m/s)	P-wave velocity (m/s)		BTS (MPa)		K_{Ic} (MPa.m ^{1/2})		FBP (MPa)	
		Dry	Sat	Dry	Sat	Dry	Sat	Dry	Sat
Rift	1.09E-10	3394	5061	7.72	7.52	1.048	1.075	7.81	7.68
Grain	8.34E-11	3610	5158	9.43	8.58	1.211	1.151	8.91	8.65
Hardway	7.20E-11	4267	5883	10.22	9.45	1.583	1.492	-	-

“Dry” and “sat” represent the initially dry and saturated samples. FBP means fracture breakdown pressure, and was measured on 50-mm-diameter granite cores at 100 mm³/s injection rate, without confining pressure. For details about testing methods, we refer to Zhuang et al. (2019a, 2020)

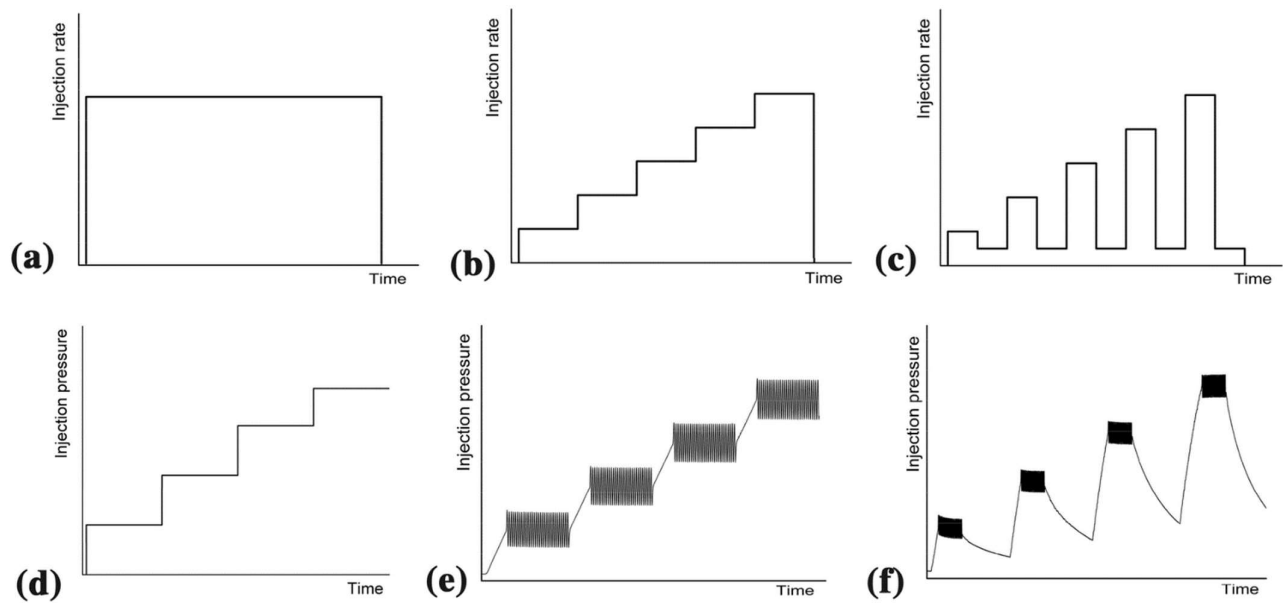


Figure 3. Six different injection schemes applied in hydraulic fracturing experiments. **a** Constant rate continuous injection (CCI), **b** stepwise rate continuous injection (SCI), **c** cyclic progressive injection (CPI), **d** stepwise pressurization (SP), **e** stepwise pulse pressurization (SPP), **f** cyclic pulse pressurization (CPP)

This is termed as stepwise pulse pressurization (SPP). Figure 3f shows cyclic pulse pressurization (CPP) which is a modification of the SPP scheme, where the injection pressure was lowered after the pulse pressurization in each cycle. The pressurization rate was 0.3 MPa/s for the SP, SPP and CPP schemes.

2.4 Injectivity, Permeability and Fracture Measurement

Hydraulic fracturing treatments are used to increase the productivity or injectivity of the reservoir. The injectivity index refers to the rate at which fluid can be injected into a well at a given pressure differential; the productivity index defines the rate at which fluid can be produced at a given pressure differential between the reservoir and the wellbore. The indices were also applied in EGS fields for evaluating the hydraulic performance of reservoirs (Nami et al. 2008; Zimmermann et al. 2009, 2010; Blöcher et al. 2016) and laboratory experiments (Zhuang et al. 2018a, 2019b). In this study, injectivity is measured through an injection test on the cubic specimen before and after hydraulic fracturing. The laboratory scale injectivity describes the hydraulic performance of a single or multiple small fractures, dictated by the fracture properties (such as length, height, aperture, roughness, and tortuosity). The field scale injectivity

describes the hydraulic performance of a fracture network or rock mass, which is additionally influenced by the connection and hydraulic communication of natural fracture sets, local inhomogeneities and near-wellbore phenomena.

In this study, injectivity measurement was combined with saturation process of rock samples. Effect of water saturation on breakdown pressure of the Pocheon granite can be ignored; however, hydraulic fracture morphology is different for the initial dry and saturated samples (Zhuang et al. 2020). We refer to our previous study that the Pocheon granite sample can be saturated, though could not be 100% saturated, by fluid injection at a very low rate and long duration (Zhuang et al. 2019a). After applying the in-situ stresses, the specimen was saturated through a five-stage injection using five different injection rates of 2, 4, 6, 8 and 10 mm³/s, which are low enough to avoid any pressure-induced failure in the specimen. Water will enter the open defects in the sample through long injection at a low rate and injection pressure. This way is workable for the Pocheon granite used in the study, which contains a lot of pre-existing microcracks. Injection pressure remains constant once the amount of fluid flowing in equals the amount of fluid flowing out (Zhuang et al. 2019a). The five plateau values of injection pressure in horizontal axis were plotted with

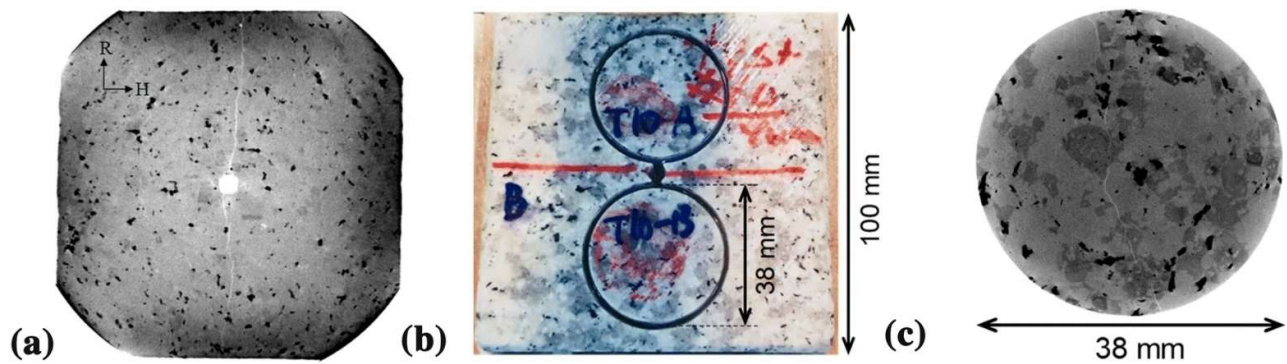


Figure 4. *a* CT image showing hydraulic fractures, *b* coring after testing for permeability measurement, *c* typical CT image of cores containing hydraulic fractures

their corresponding injection rates in vertical axis, and injectivity was estimated as the slope of their linear fitting curve. After the hydraulic fracturing test, injectivity was measured again using an injection test at injection rates of 5, 10, 15, 20, 25 and 30 mm³/s. The same tap water having a viscosity of around 1.0 mPa·s at the room temperature of 20°C was used through the experiments, including the saturation process, fracturing and the injectivity measurement after fracturing.

After measuring the injectivity, X-ray computed tomography (CT) was applied to observe three-dimensional structures of the hydraulic fractured samples using an industrial CT device. The X-ray attenuation value (i.e., CT number) is proportional to the relative density of a constituent material; therefore, the spatial variability of the CT number naturally demonstrates how microstructural features are clustered and thus enables visualization and quantification of the hydraulic fractures in the samples. The image resolution for the 100-mm cube was 117 μm of pixel pitch for the X-ray energy with a voltage of 230 kV and an electric current of 1200 mA (Fig. 4a). The resolution was 34 μm for 38 mm diameter cores scanned at 120 kV and 200 mA (Fig. 4c). In all cases, fractures were only generated in the upper part of the specimen. Then, cylindrical samples with 38 mm diameter and 100 mm height were cored parallel to the vertical principal stress axis from the cubic specimen, as shown in Fig. 4b. The core sample was further cut into two samples, each with a height of approximately 32–38 mm, where the upper part contains the hydraulic fracture while the lower part does not, as confirmed by CT scans (Fig. 4c). The pair of two core samples with and

without hydraulic fractures, obtained from the same sample, were then used for permeability testing to compare how much permeability was improved by hydraulic fracturing. Finally, a thin section was obtained at 5 mm below the top surface of the core samples containing hydraulic fractures, for further microscopic observation and fracture geometry measurement.

3 Experimental Results and Analysis

3.1 Summary of the Main Test Results

Test conditions and the major results of a total of 20 test cases are summarized in Table 2. Each specimen was given an identification number for reference. For the same injection scheme, injection parameters, such as injection rate, pressure amplitude and frequency, were varied to investigate their influence on fracturing results. These parameters are also included in the table. The injected volume represents the total volume of water pumped into the sample, while the volume of outflow, due to limited sample size, is not measurable. The injected fluid did not accumulate in the sample once it was saturated because of the limited sample size and drainage at its boundary surfaces. Therefore, the influence of the total injected volume was not investigated in this study, although it is thought to be an important factor affecting the occurrence of the largest magnitude of induced seismicity in geothermal stimulation (McGarr 2014). Instead, we investigated other important parameters in a hydromechanically coupled process, such as BP, maximum AE amplitude obtained from the hydraulic fracturing test, injectivity before and after fracturing, the fold of increase (FOI) for injectivity obtained from injection tests and the

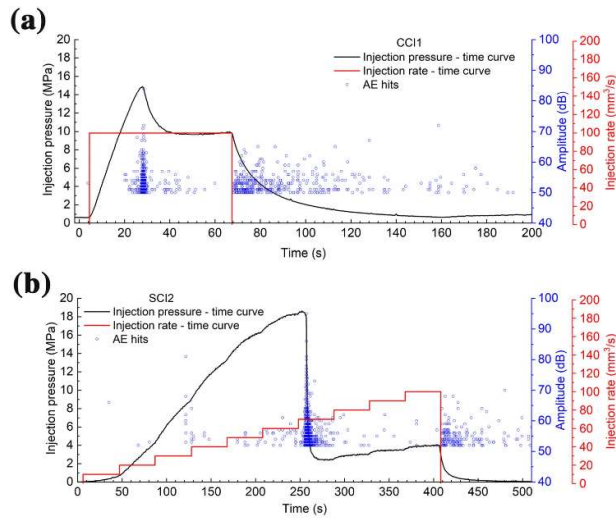


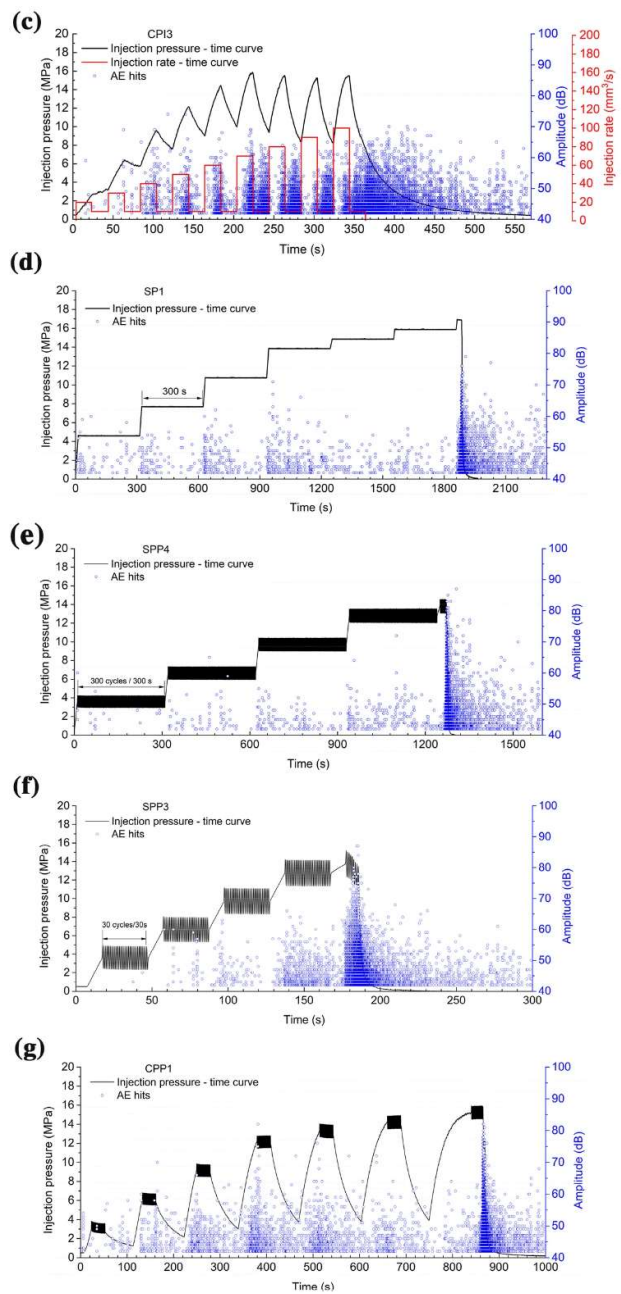
Figure 5. Typical injection pressure/injection rate–time curves and acoustic emissions (AEs): **a** specimen CCI1, **b** specimen SCI2, **c** specimen CPI3, **d** specimen SP1, **e** specimen SPP4, **f** specimen SPP3, and **g** specimen CPP1

FOI for permeability obtained from additional permeability testing. The tests could not be performed with constant volume or constant hydraulic energy for the reasons explained above. Instead, each test was stopped after macroscopic breakdown and the injection rate was increased to a maximum magnitude of 100 mm³/s in the SCI and CPI injection schemes.

3.2 Injection Pressure–Time Curves and AE Monitoring Results

Figure 5a–f shows typical injection pressure and injection rate variations with time together with amplitude of AE hits for the six different injection schemes. Specimen CCI1 was fractured after approximately 24 s of injection at a constant rate of 100 mm³/s. AE clusters were detected before and after the breakdown, and the AE with the maximum amplitude of 84 dB occurred almost right at the time of breakdown. The injection pressure decreased from the peak value of 14.91 MPa to approximately 10 MPa, where it converged. Afterward, injection was stopped at 63 s, and more AE clusters occurred during the shut-in period, which gives the same phenomenon for all cases.

For the stepwise rate continuous injection in Fig. 5b, the injection rate was increased by 10 mm³/s in each step until the target value of 100 mm³/s is reached. Breakdown was observed during the injection stage at a rate of 70 mm³/s for specimen SCI2, and the injection



pressure instantly dropped to approximately 2 MPa. If the fracture propagated completely to the outside boundary, the pressure should drop to zero as hydrostatic pressure was not considered in the experiments. The maximum amplitude of AE occurred immediately at breakdown.

For the cyclic progressive injection case of specimen CPI3 (Fig. 5c), high injection rates from 20 to 100 mm³/s and the fixed low injection rate of 10 mm³/s alternate for each cycle. Failure occurs at the 6th cycle during injection at the high injection rate of 70 mm³/s, as supported by AE clusters with relatively high amplitudes and a decrease in the maximum injection

Table 2**Summary of main test conditions, test results and additional measurements for all 20 testing cases using six different injection schemes**

Injection scheme	Specimen no	Injection parameters	Injected volume /mm ³	BP/MPa	Max. AE Ap/dB	/mm ³ (s MPa) ⁻¹			
						Inj. Before	Inj. After	Inj. FOI	Perm. FOI
Constant rate continuous injection (4 cases)	CCI1	IR 100	6300	14.91	84	2.14	4.88	2.3	-
	CCI2	IR 50	22,300	16.23	61	2.01	2.27	1.1	-
	CCI3	IR 400	6800	18.51	90	1.84	10.99	6.0	2.1
	CCI4	IR 400	61,200	15.37	88	3.25	-	-	4.6
Stepwise rate continuous injection (2 cases)	SCI1	IR 10-100	18,000	15.62	82	3.02	4.97	1.6	-
	SCI2	IR 10-100	18,000	18.63	95	2.05	15.93	7.8	12.0
Cyclic progressive injection (6 cases)	CPI1	High IR 20-100	Dr 20 12,400	19.23	77	2.12	2.87	1.4	-
	CPI2	Low IR 10	Dr 20 12,400	17.51	75	2.31	3.16	1.4	-
	CPI3		Dr 20 12,600	15.86	74	2.12	2.74	1.3	-
	CPI4		Dr 40 25,200	14.13	82	2.41	3.71	1.5	1.2
	CPI5		Dr 60 37,800	18.01	74	2.16	3.26	1.5	-
	CPI6		Dr 60 37,800	17.91	80	1.83	5.76	3.1	1.2
Stepwise pressurization (1 case)	SP1	PR 0.3/Dr 300	26,950	16.94	79	2.51	9.88	3.9	-
Stepwise pulse pressurization (4 cases)	SPP1	Ap 1.2/Fq 2/Dr 30	6125	16.28	87	2.13	32.77	15.4	8.6
	SPP2	Ap 2.4/Fq 1/Dr 30	8575	16.63	85	1.99	26.72	13.4	8.2
	SPP3	Ap 2.4/Fq 1/Dr 30	9800	15.20	87	2.27	27.28	12.0	-
	SPP4	Ap 1.2/Fq 1/Dr 300	28,910	14.57	87	2.24	30.70	13.7	2.7
Cyclic pulse pressurization (3 cases)	CPP1	Ap 1.2/Fq 1/Dr 30	12,850	15.96	82	1.57	14.84	9.5	-
	CPP2	Ap 1.2/Fq 1/Dr 30	4883	13.01	74	1.63	3.87	2.4	-
	CPP3	Ap 0.8/Fq 2/Dr 30	12,000	15.79	80	1.57	8.94	5.7	-

IR injection rate (mm³/s), PR pressurization rate (MPa/s), BP breakdown pressure (MPa), AE acoustic emission, Ap amplitude (dB), Fq frequency (Hz), Dr injection duration (s), Inj. Injectivity (mm³ (s MPa)⁻¹), Perm. permeability, FOI fold of increase

pressure between the 6th cycle and the 7th cycle. The maximum AE amplitude of 74 dB was observed at a relatively early stage of two injection cycles before the obvious failure inferred from the injection pressure curve.

Figure 5d shows the only case of SP under a constant pressurization rate. The injection pressure was increased by approximately 3 MPa in the previous four stages at a rate of 0.3 MPa/s, and 1 MPa for the last three stages as the specimen approached a failure. In each stage, the peak pressure was maintained for 300 s. The specimen SP1 failed during the pressurization of the 7th stage, and the injection was stopped.

Figures 5e shows the case of specimen SPP4, where pulse pressurization was applied with an amplitude of 1.2 MPa, frequency of 1.0 Hz and a duration of 300 s. The difference between the case of SPP4 and the case of SP1 having the same duration of 300 s in each stage is that pulse pressurization was not applied for the latter. The duration and amplitude were varied in the other three cases to investigate their influence on the hydraulic fracturing behavior.

For specimen SPP3, a pressure amplitude of 2.4 Pa and a duration of 30 s were applied, as shown in Fig. 5f. Both specimens SPP3 and SPP4 failed during the 5th stage of pulse pressurization. Number of AE clusters increases with increasing stage number, indicating the accumu-

lated local failure of the specimens.

Figure 5g shows specimen CPP1 after pulse pressurization with an amplitude of 1.2 MPa, frequency of 1.0 Hz and duration of 30 s. It was applied at the peak pressure for each cycle, and after that, the injection pressure was lowered to very small magnitudes compared to the peak values. The specimen CPP1 was fractured during the pulse pressurization at the 7th cycle and, accompanied by AE clusters, including the largest one with amplitude of 82 dB.

3.3 Breakdown Pressure, Injectivity and Maximum AE Amplitude

Figure 6 shows the three important indices for hydraulic fracturing results in all cases: (1) BP or the maximum injection pressure, (2) the fold of increase (FOI) for injectivity and (3) the maximum amplitude of AE. BP varies from the lowest value of 13.01 MPa to the highest value of 19.23 MPa. The granite used in this study contains many heterogeneously distributed pre-existing microcracks and behaves anisotropic. Variability in the Brazilian tensile strength and hydraulic breakdown pressure of 50 mm diameter core samples are reported to be 1~2 MPa (Zhuang et al. 2020). The magnitudes are believed to be amplified when sample size gets larger. Considering the heterogeneity of samples, differences in BPs for different injection

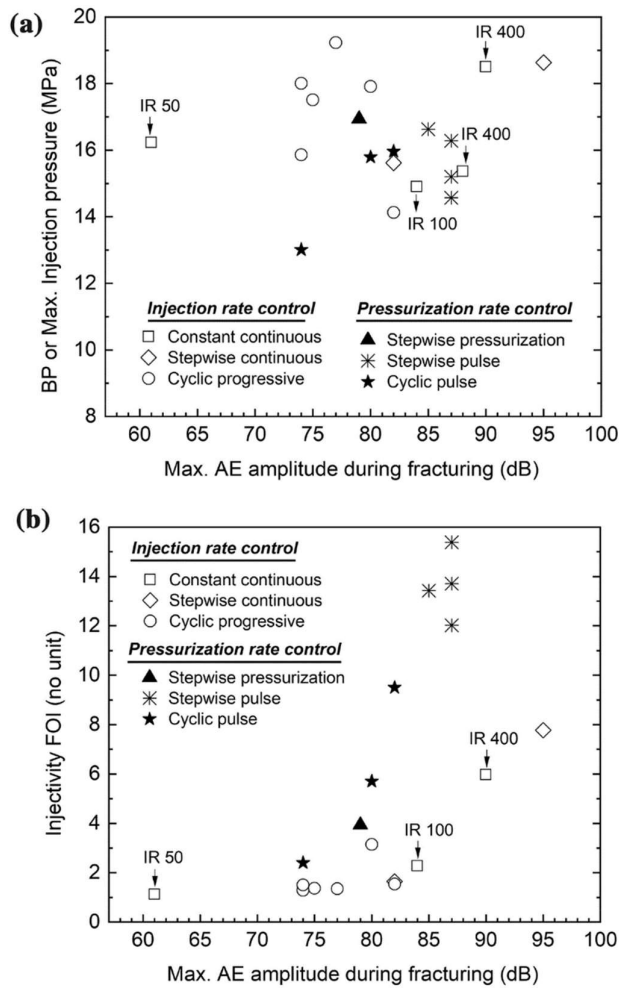


Figure 6. Comparison of **a** BP or the maximum injection pressure and **b** Fold of Increase (FOI) for injectivity, plotting with the maximum amplitude of AE hits in each case. IR injection rate

schemes compared at either injection rate control or pressurization rate control are insignificant. The decrease of BP by $\sim 20\%$ with increasing cycle number was confirmed in 50 mm-diameter cylinders of the same Pocheon granite. An upper limit of injection pressure lower than the monotonic BP was set during cyclic injection, and the sample was fractured by increasing number of cycles from several to hundreds (Zhuang et al. 2019b). In this study, for the cyclic progressive injection, injection rate was increased to the maximum value of $100 \text{ mm}^3/\text{s}$ by a total of nine cycles, and in each cycle the increment in injection rate was $10 \text{ mm}^3/\text{s}$. As a result, there is no obvious BP reduction due to limited number of cycles. Nevertheless, the maximum AE amplitude tends to increase with increasing BP or the maximum injection pressure when compared at the same injection scheme, except

for the stepwise pulse pressurization.

Injectivity FOI and the maximum amplitude of AE are plotted in Fig. 6b. Out of the six injection schemes, the four cases of stepwise pulse pressurization show significantly larger FOIs of approximately 12~16 compared to other injection schemes applied. The six cases of cyclic progressive injection show low maximum amplitude of AE and injectivity increase. Similar findings showing that cyclic injection helps to reduce induced seismicity while having limitations in terms of permeability enhancement are reported by Zhuang et al. (2019b) and Zimmermann et al. (2018). Hydraulic fractures created by CHF compared to HF were relatively shorter and had smaller apertures, despite covering a broader area. When we combine the pulse pressurization with cyclic injection, it was found that the injectivity FOI was largely improved with the maximum and average FOI of 9.5 and 5.9, respectively. The FOIs are about three times more compared to the maximum and average FOI (3.1 and 1.7) in cyclic progressive cases and are still more than the FOIs (7.8 and 3.8) for continuous injection cases, regardless of constant rate or stepwise rate.

For the CPI cases, the duration of injection at both high and low injection rates increased from 20 to 40 s and then to 60 s. The average injectivity FOI for the duration of 20, 40 and 60 s was 1.37, 1.5 and 2.3, respectively. A small increase in injectivity FOI was observed with increasing duration of injection. Past studies show that longer duration of injection (or lower frequency) results in greater fracturing radius (Wu et al. 2016), higher AE energy release and higher intensity of fracture extension (Xu et al. 2017) for progressive PHF in coalbed methane reservoir. Moreover, the pressure amplitude is assumed to have an influence as well.

Permeability measurements were not available for all specimens. The results of eight cases show that permeability FOI ranges from 1.2 to 12.0, as listed in Table 2. Some specimens have high-permeability FOI, while the injectivity FOI was low, and vice versa. This is because the injectivity evaluates the hydraulic performance of the integral specimen, while the permeability was measured on a 38 mm diameter core sample extracted from the specimen.

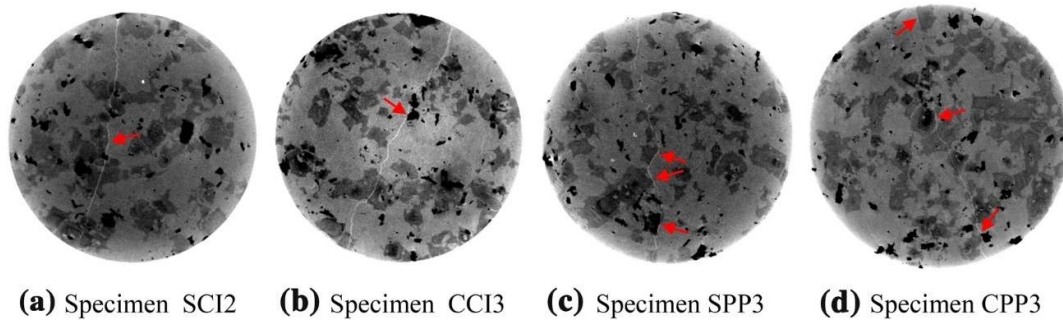


Figure 7. Typical CT slices showing fractures in 38 mm diameter core samples. Black grains: mica; dark grey grains: feldspar, distinction between different types of feldspar like microcline and orthoclase is difficult in the current image; light grey: quartz (mostly) mixed with feldspar; white line: fracture. The arrows note the places of fractures along the mineral boundary (intergranular fracture)

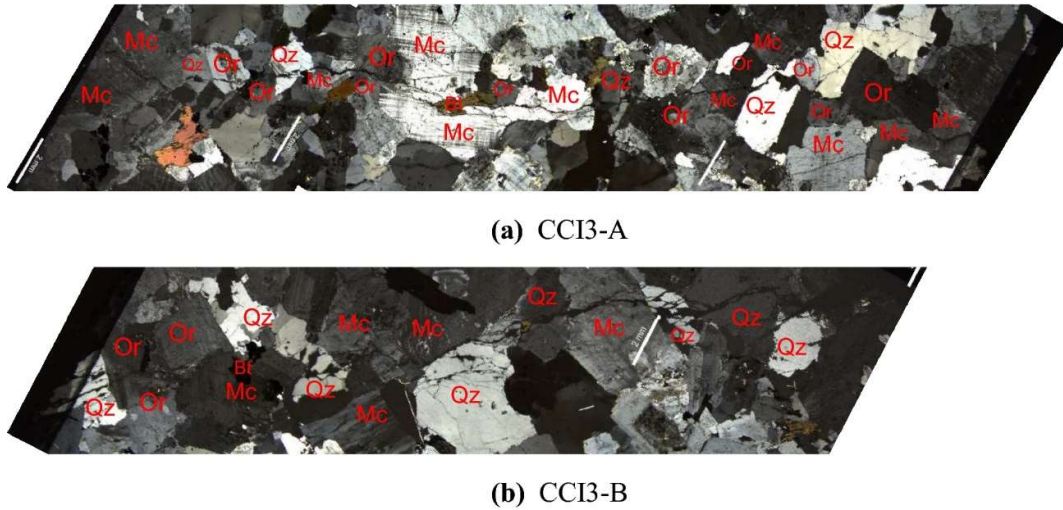


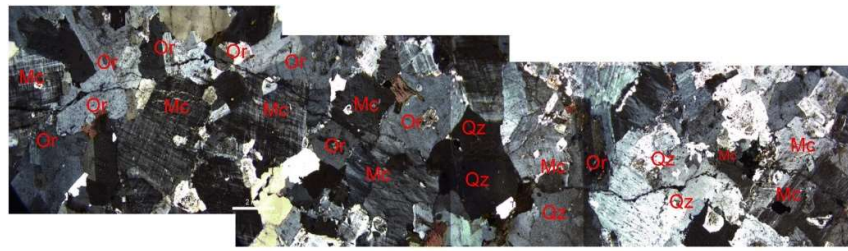
Figure 8. Thin section with mineral identification along hydraulic fractures generated at both sides of the borehole in specimen CCI3

4 Hydraulic Fracture Observation at Grain-Scale

A CT scan confirmed that in most cases, bi-wing fractures, as shown in Fig. 4a, were generated parallel to the maximum horizontal stress as well as the rift plane. A CT scan on the 38 mm-diameter core sample allows a closer observation of fractures at the grain scale. Typical CT slices showing hydraulic fractures in the 38 mm-diameter core sample are shown in Fig. 7. Both intergranular and intragranular fractures were observed, as also reported by Zhuang et al. (2018a, b). Intragranular fractures cutting across mineral grains with a clear aperture are thought to be tensile dominated (Chen et al. 2015), while intergranular fractures could be either tensile or shear. Figure 7c shows a case in which intergranular fractures develop along mineral boundaries, curved as noted by arrows, and contribute to the tortuosity of fracture. Here

the tortuosity is defined as the ratio of the total length along fracturing path and the linear distance between the two ends of the fracture. Past study has reported that the tortuosity of hydraulic fractures in Kurokami-jima granite fractured by water is around 1.10, and it decreases with increasing fluid viscosity (Chen et al. 2015).

Thin section analysis was conducted on typical core samples for detailed analysis of fractures at the grain scale. Figure 8a, b shows the two fractures on the left and right sides of the borehole from the top view of specimen CCI3 having been fractured by continuous injection at a constant rate. The “multi-point” and “measure” tools embedded in the open access software ImageJ are employed to measure fracture length. For the left-side fracture noted as CCI3-A, the total length was measured to be 35.89 mm. The fracture mainly cuts across microcline (Mc), orthoclase (Or) and quartz (Qz) grains,

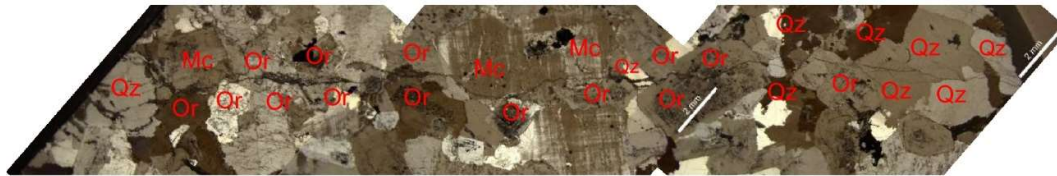


(a) SPP4-A

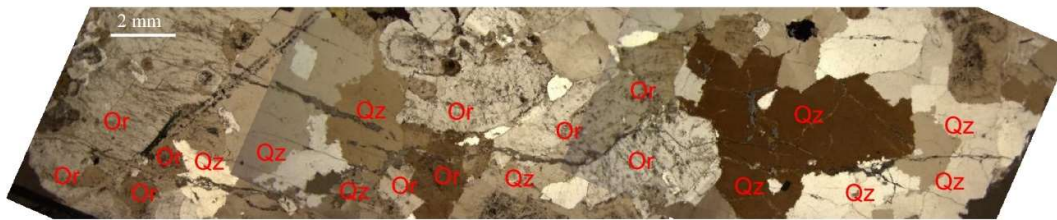


(b) SPP4-B

Figure 10. Thin section with mineral identification along hydraulic fractures generated at both sides of the borehole in specimen SPP4



(a) CPP1-A



(b) CPP1-B

Figure 9. Thin section with mineral identification along hydraulic fractures generated at both sides of the borehole in specimen CPP1

corresponding to a fraction of 41.0%, 25.9% and 18.4%, respectively. Intergranular fractures of Qz-Or, Or-Mc, and Or-Or were observed, and these fractures occupied 14.8% of the total length. Figure 8b shows the right side of fracture CCI3-B, where a distinct phenomenon is observed that quartz grains are more fractured than microcline, and orthoclase grains and quartz chips frequently exist inside or beside the main fracture. This is thought to be related to pre-existing microcracks abundant in quartz grains. This is presumably because the main fracture path is preferably aligned parallel to the orientation of intragranular microcracks within quartz grains in the rift plane, and the injected fluid pressure results in high localized

tensile stresses acting on the main hydraulic fracture as well as nearby microcracks. This phenomenon could benefit permeability enhancement because the local damage zone is relatively larger than the zones with only a single fracture, and the fracture will not close completely after shut-in, assuming that rock chips are generated from fracturing and remain inside fracture.

Figure 9 shows two fractures in specimen SPP4 fractured by stepwise pulse pressurization. The fracture SPP4-A in Fig. 9a has the largest tortuosity of 1.103 of all 18 measured cases. The fracture started and ended both with intragranular fractures in microcline grains and intergranular fractures of Mc-Or and Mc-Qz. In

Table 3**Comparison of fracture measurements and the maximum AE amplitude for all 18 fractures from the 10 selected fractured specimens**

Specimen	Single fracture length (mm)	Average by injection scheme (mm)	Tortuosity	Intragranular fracture			Intergranular fracture	Max. AE amplitude (dB)
				Mc	Or	Qz		
CCI3-A	35.89	32.0	1.062	41.0%	25.9%	18.4%	14.8%	90
CCI3-B	28.17	1.050	32.8%	11.9%	48.2%	7.1%		
SCI2-A	33.78	32.0	1.032	14.0%	34.4%	35.9%	15.7%	95
SCI2-B	30.27	1.043	16.5%	20.7%	40.3%	22.5%		
CPI5	16.12	16.1	1.094	0	47.8%	44.3%	7.9%	74
SP1	19.71	19.7	1.038	6.0%	63.7%	0	30.3%	79
SPP1-A	38.18	38.8	1.025	21.9%	22.4%	33.7%	22.0%	87
SPP1-B	41.34		1.045	16.1%	45.4%	34.1%	4.4%	
SPP2-A	37.18		1.059	21.5%	30.8%	39.5%	8.2%	85
SPP2-B	46.22		1.041	15.4%	31.8%	38.0%	14.8%	
SPP3-A	31.58		1.078	23.5%	60.1%	16.1%	0.3%	87
SPP3-B	32.62		1.026	6.7%	28.1%	41.5%	23.7%	
SPP4-A	44.09		1.103	35.5%	24.7%	17.6%	22.2%	87
SPP4-B	38.87		1.079	13.0%	33.3%	36.1%	17.6%	
CPP1-A	33.07	30.7	1.043	6.1%	39.5%	34.4%	20.0%	82
CPP1-B	32.01		1.061	0%	39.7%	51.7%	8.6%	
CPP3-A	23.68		1.083	4.9%	45.0%	29.3%	20.8%	80
CPP3-B	34.16		1.070	0%	80.8%	16.5%	2.7%	

A and B represent fractures at different sides of borehole for the same specimen. For the two cases of CPI5 and SP1 specimens, fractures were captured on only one side of borehole from the thin sections

Mc Microcline, Or Orthoclase, Qz Quartz

Fig. 9b, quartz chips are found at multiple places. Figure 10 shows fractures in specimen CPP1 having experienced cyclic pulse pressurization. The fractures in specimen CPP1 have relatively smaller apertures compared with the fractures in specimens CCI3 and SPP4; however, the interaction of hydraulic fractures and preexisting microcracks in quartz clusters resulting in relatively large damage zones are observed, particularly for the fracture side B of specimen CPP1.

Table 3 lists the measurements of 18 fractures corresponding to 10 selected specimens. The total length of the main fracture along the fracturing path, tortuosity, fractions of intragranular and intergranular fractures, and the maximum AE amplitude during fracturing are presented in the table. The total length of measured fractures varies between 16.02 mm and 46.22 mm and intragranular fractures dominated in all cases. The portion of intergranular fractures ranges from 0.3 to 30.3%. This indicates that the hydraulic fracturing of the intact granite specimens under the true triaxial stress conditions was tensile dominated. In most cases intragranular fractures were mostly cut across orthoclase or quartz grains. The tortuosity of hydraulic fractures varies from 1.025 to 1.103 for all 18 cases, with an average value of 1.057.

5 Discussion

Comparison of injectivity and fracture measurements observed in different injection schemes

merits further discussion.

First, fracture length affects hydraulic performance. Specimens subjected to the SPP scheme consistently showed relatively larger lengths of fractures than other specimens having experienced different injection schemes. The average length on eight fractures was estimated to be 38.8 mm; in particular, the fractures in specimens CPI5 and SP1 corresponding to the lowest AE amplitudes of 79 dB and 74 dB among the ten specimens are obviously shorter compared to those in other cases. Zhuang et al. (2018a, 2019b) reported that the low injectivity measured on fractured samples was attributed to their short length and the small aperture of the fractures. When comparing the two cases of specimens SP1 and SPP4, in which the only difference in test conditions is the pulse pressurization applied on specimen SPP4 at the peak injection pressure of each stage, the fractures in the latter are two times longer and the injectivity of the fractured specimens are three times higher. Similarly, the CPP scheme shows a much better injectivity enhancement compared to the CPI scheme, with the average injectivity FOI of 5.7 for CPP and 1.7 for CPI. Moreover, the average fracture length corresponding to the SPP scheme (38.8 mm) is also larger than that for the CPP scheme (30.7 mm). In conclusion, all observations show that pulse pressurization helps to propagate the fracture, leading to longer fractures and higher injectivity, particularly under the condition that injection pressure is stepwise continuously increased without depressurization.

Second, cyclic injection tends to form fracture paths of least resistance. CPI and CPP injection schemes (specimens CPI5, CPP1 and CPP3) show consistently smaller portions (0 and 4.9%) of intragranular fractures cutting microcline grains compared to those of high magnitudes of 14.0–41.0% in the CCI and SCI schemes and 6.7–35.5% in the SPP scheme. Quartz grains have the lowest tensile strength among the three main types of grains as microcracks are well developed in quartz-rich rock as opposed to microcline and orthoclase grains. Microcline forms during slow cooling of orthoclase and is more stable at lower temperatures than orthoclase. The microcline grains could have higher tensile strength than orthoclase grains; however, further evidence is needed to confirm this assumption. Cyclic injection promotes energy efficiency in HF as it avoids wasting energy in forming intragranular cracks in mineral grains with relatively high strength. Results of our previous study has shown that cyclic injection creates more intergranular fractures compared to continuous injection (Zhuang et al. 2018a). The tensile strength at the grain boundaries is usually lower than splitting of grains (Savanick and Johnson 1974) and, therefore, intergranular fractures are preferred.

Third, preexisting microcracks in granite have significant influence on the hydraulic fracturing result. Quartz grains in Pocheon granite are more fractured than orthoclase and microcline grains. Results presented in Fig. 8b show that rock chips of quartz grains were frequently observed inside hydraulic fractures, particularly when quartz grains are adjacent to orthoclase or microcline grains. Moreover, as shown in Fig. 10, fracture branching and interaction of hydraulic fractures and preexisting microcracks are observed in quartz clusters in the sample CPP1. These observations are confirmed in other cases regardless of the injection scheme, although the frequency of occurrence varies from case to case. As preexisting microcracks are abundant in the Pocheon granite (Zhuang et al. 2016, 2019a), the chips formed are likely created when hydraulic fractures interacted with microcracks in quartz grains, resulting in crisscrossed fractured quartz grains. This will help to enlarge the damage zone and improve the permeability increase. At a laboratory scale,

we hypothesize that the optimized hydraulic fractures for intact granite specimens are promoting to connect these microcracks, to form a relatively large damage zone. Ishida et al. (2000) deduced from laboratory testing that the shear type micro-fracturing observed in cubic granite specimens with large grains (average grain sizes of 0.88 mm and 1.12 mm) is expected to occur mainly through the connection of tips of preexisting defects lying along a rift plane. Naturally fractured rock mass is highly inhomogeneous and contains geological discontinuities at various length scales (Zhang et al. 2019). The influence of microcracks at a core scale on hydraulic fracturing is analogous to the influence of natural fractures to hydraulic stimulation in the field. Quartz chips were also found in supercritical CO₂ fractured granite sample (Ishida et al. 2016).

Fourth, next on the above discussion, correlation between rock chips (natural proppants) and pulse pressurization needs further investigation. Researchers have noted that rock chips or spalls (and rock chunks under certain conditions) associated with the fracturing processes could influence the local stress field near hydraulic fractures and fracture propagation (Kiel 1977; Zang et al. 2019). Additional increase in permeability can result from rock chips moving with the fluid to the fracture tip, causing local stress redistributions favoring the arrest and branching of fractures (Kiel 1977). This so-called Kiel process proposed as a method for creating dendritic (branching) fracture system was developed to enhance oil production in sedimentary rocks, and its fracturing mechanism does not fit hard and low-permeability granitic rocks. In contrast to the deduction by Kiel (1977) that rock chips and chunks are produced due to the spalling of fracture walls during the shut-in phase, Zang et al. (2019) assume that rock chips are removed from the fracture walls through high-frequency vibrations loaded by a secondary pump (pulse pressurization) during fatigue hydraulic fracturing. Neither study has reported the specific mineral type of rock chips, or has provided further evidence to confirm the formation process of rock chips and their movement with fluid. In this study, we confirmed that the rock chips are mostly from quartz grains and a few from orthoclase grains. Due to limited

testing cases, it is hard to correlate generation of more rock chips with pulse pressurization compared to other injection schemes. We suspect that these rock fragments are not plugging the fracture but instead act as stress concentrator at the fracture tip for further persistent fracture growth, which has resulted in relatively larger fracture lengths for injection schemes applying pulse pressurization (SPP and CPP), compared to those without pressure pulses (SP and CPI). We see further studies on natural rock proppants generated during the hydraulic fracturing process with advanced injection protocols as key to understand the evolution of the process and damage zone associated with fluid-driven fracture growth.

6 Conclusions

We perform laboratory hydraulic fracturing tests of Pocheon granite under six different injection schemes. The hydraulic performance of fractured samples is evaluated through measurements of breakdown pressure, injectivity, permeability and fracture microscopic properties. The research findings are summarized as follows:

1. Intragranular fractures splitting microcline, orthoclase and quartz grains dominated the hydraulic fractures irrespective of the injection scheme. This indicates a tensile fracturing mechanism for the intact granite specimens tested under true triaxial stress conditions.
2. Stepwise pulse pressurization (SPP) creates the largest fracture length and results in the best injectivity enhancement among the six injection schemes tested.
3. Cyclic pulse pressurization (CPP) is superior to the other five injection schemes considering the hydraulic performance improvement as well as induced seismicity reduction. The effects of the key parameters like the amplitude and frequency of pulse pressurization remain to be investigated for the optimization of the fracturing results.
4. Cyclic progressive injection (CPI) shows the lowest average magnitude of the maximum AE amplitude among the six schemes, while improvement in injectivity and permeability is the least pronounced.

5. Grain-scale observation of hydraulic fractures show that quartz grains are more fractured than microcline and orthoclase grains, and quartz chips are frequently observed inside hydraulic fractures. Injection schemes applying cyclic injection rather than continuous injection tend to create much smaller portions of intragranular fractures in microcline grains.

Acknowledgements This work has been supported by the Korea-EU Joint Research Support Program of Korea Institute for Advancement of Technology (KIAT) under Grant Agreement No. N0002098, the National Research Foundation of Korea (NRF) through a Grant (No. NRF-2015K1A3A7A03074226) in the framework of the European Union's Horizon 2020 Research and Innovation Programme under Grant Agreement No. 691728, the International Collaborative Research Project (20190282-001) funded by Korea Institute of Civil Engineering and Building Technology (KICT), and the NRF-NSFC Cooperation Program through a Grant (2018K2A9A2A06021342).

References

- Blöcher G, Reinsch T, Hennings J, Milsch H, Regenspurg S, Kummerow J, Francke H, Kranz S, Saadat A, Zimmermann G, Huenges E (2016) Hydraulic history and current state of the deep geothermal reservoir Groß Schönebeck. *Geothermics* 63:27–43
- Chen Y, Nagaya Y, Ishida T (2015) Observations of fractures induced by hydraulic fracturing in anisotropic granite. *Rock Mech Rock Eng* 48:1455–1461
- Dehkhoda S, Hood M (2013) An experimental study of surface and sub-surface damage in pulsed water-jet breakage of rocks. *Int J Rock Mech Min Sci* 63:138–147
- Diaz MB, Jung SG, Zhuang L, Kim KY (2018a) Comparison of acoustic emission activity in conventional and cyclic hydraulic fracturing in cubic granite samples under triaxial stress state. In: *Proceedings of the 52nd US Rock Mechanics/Geomechanics Symposium*, Seattle, ARMA 18–1160
- Diaz MB, Jung SG, Zhuang L, Kim KY, Zimmermann G, Hofmann H, Zang A, Stephansson O, Min KB. (2018b) Hydraulic, mechanical and seismic observations during hydraulic fracturing by cyclic injection on Pocheon granite. In: *Proceedings of the 10th Asian Rock Mechanics Symposium*, Singapore, paper No. 368
- Diaz M, Jung SG, Zhuang L, Kim KY, Hofmann H, Min KB, Zang A, Zimmermann G, Stephansson O, Yoon JS (2018c) Laboratory investigation of hydraulic fracturing of granite under true triaxial stress state using different injection schemes – Part 2. Induced seismicity. In: *Proceedings of International Conference on Coupled Processes in Fractured Geological Media: Observation, Modeling, and Application*, Wuhan
- Douglass PM, Voight B (1969) Anisotropy of granites: a reflection of microscopic fabric. *Geotechnique* 19:376–398

- Grigoli F, Cesca S, Rinaldi AP, Manconi A, López-Comino JA, Clinton JF, Westaway R, Cauzzi C, Dahm T, Wiemer S (2018) The November 2017 M_w 5.5 Pohang earthquake: a possible case of induced seismicity in South Korea. *Sci* 360(6392):1003–1006
- Guo F, Morgenstern NR, Scott JD (1993) An experimental investigation into hydraulic fracture propagation—Part 1. Experimental facilities. *Int J Rock Mech Min Sci Geomech Abstr* 30(3):177–188
- Haimson B, Fairhurst C (1969) Hydraulic fracturing in porous-permeable materials. *J Petrol Tech* 21:811–817
- Hofmann H, Zimmermann G, Zang A, Min KB (2018) Cyclic soft stimulation (CSS): a new fluid injection protocol and traffic light system to mitigate seismic risks of hydraulic stimulation treatments. *Geotherm Energy* 6:27
- Hofmann H, Zimmermann G, Zang A, Yoon JS, Stephansson O, Kim KY, Zhuang L, Diaz M, Min KB (2018b) Comparison of cyclic and constant fluid injection in granitic rock at different scales. In: *Proceedings of the 52nd US Rock Mechanics/Geomechanics Symposium*, San Francisco, ARMA 18–691
- Hofmann H, Zimmermann G, Farkas M, Huenges E, Zang A, Leonhardt M, Kwiatek G, Martinez-Garzon P, Bohnhoff M, Min KB, Fokker P, Westaway R, Bethmann F, Meier P, Yoon KS, Choi JW, Lee TJ, Kim KY (2019) First field application of cyclic soft stimulation at the Pohang Enhanced Geothermal System site in Korea. *Geophys J Int* 217:926–949
- Hunt WC, Shu WR (1989) Controlled pulse fracturing for well stimulation. In: *Proceedings of the SPE symposium on low permeability reservoirs*. Denver, Colorado, Paper No. 18972-MS
- Ishida T, Sasaki S, Matsunaga I, Chen Q, Mizuta Y (2000) Effect of grain size in granitic rocks on hydraulic fracturing mechanism. *Trends in Rock Mechanics (Proc. of Sessions of Geo-Denver 2000)*. *Geotech Spec Publ ASCE* 102:128–139
- Ishida T, Chen Y, Bennour Z, Yamashita H, Inui S, Nagaya Y, Naoi M, Chen Q, Nakayama Y, Nagano Y (2016) Features of CO₂ fracturing deduced from acoustic emission and microscopy in laboratory experiments. *J Geophys Res Solid Earth* 121:8080–8098
- Kiel OM (1977) The Kiel process—reservoir stimulation by dendritic fracturing. *Society Petroleum Engineers AIME*, paper SPE-6984-MS, p 29
- Li Q, Lin B, Zhai C (2014) The effect of pulse frequency on the fracture extension during hydraulic fracturing. *J Natural Gas Sci Eng* 21:296–303
- Majer EL, Baria R, Strark M, Oates S, Bommer J, Smith B, Asanuma H (2007) Induced seismicity associated with enhanced geothermal systems. *Geothermics* 36:185–222
- McGarr A (2014) Maximum magnitude earthquakes induced by fluid injection. *J Geophys Res Solid Earth* 119:1008–1019
- Meier PM, Rodríguez A, Bethmann F (2015) Lessons learned from Basel: new EGS projects in Switzerland using multistage stimulation and a probabilistic traffic light system for the reduction of seismic risk. In: *Proceedings of the World Geothermal Congress*, Melbourne
- MISTRAS Group Inc (2014) Express-8 AE System User's manual. Physical Acoustic Corporation
- Nami P, Schellschmidt R, Schindler M, Tischner T (2008) Chemical stimulation operations for reservoir development of the deep crystalline HDR/EGS system at Souzous-Forêts (France). In: *Thirty-Second Workshop on Geothermal Reservoir Engineering*. Stanford, Paper SGP-TR-185
- Patel SM, Sondergeld CH, Rai CS (2017) Laboratory studies of hydraulic fracturing by cyclic injection. *Int J Rock Mech Min Sci* 95:8–15
- Savanick GA, Johnson DI (1974) Measurement of the strength of grain boundaries in rock. *Int J Rock Mech Min Sci Geomech Abstr* 11:173–180
- Stanchits S, Surdi A, Edelman E, Suarez-Rivera R (2012) Acoustic emission and ultrasonic transmission monitoring of hydraulic fracture initiation and growth in rock samples. In: *Proceedings of 30th European Conference on Acoustic Emission Testing and 7th International Conference on Acoustic Emission*, Granada
- Stephansson O, Semikova H, Zimmermann G, Zang A (2019) Laboratory pulse test of hydraulic fracturing on granitic sample cores from Äspö HRL, Sweden. *Rock Mech Rock Eng* 52:629–633
- Wu J, Zhang SH, Cao H, Kemeny J (2016) The effect of pulse frequency on the acoustic emission characteristics in coal bed hydraulic fracturing. In: *Proceedings of the 50th US Rock Mechanics/Geomechanics Symposium*, Houston, ARMA 16–756
- Xie L, Zhuang L, Kim KY, Min KB (2018) Simulating hydraulic fracturing in low permeable rock with consideration of fluid infiltration into rock matrix. In: *Proceedings of the 10th Asian Rock Mechanics Symposium*, Singapore
- Xu J, Zhai C, Qin L (2017) Mechanism and application of pulse hydraulic fracturing in improving drainage of coalbed methane. *J Nat Gas Sci Eng* 40:79–90
- Zang A, Yoon JS, Stephansson O, Heidbach O (2013) Fatigue hydraulic fracturing by cyclic reservoir treatment enhances permeability and reduces induced seismicity. *Geophys J Int* 195(2):1282–1287
- Zang A, Stephansson O, Stenberg L, Plenkers K, Specht S, Milkereit C, Schill E, Kwiatek G, Dresen G, Zimmermann G, Dahm T, Weber M (2017) Hydraulic fracture monitoring in hard rock at 410 m depth with an advanced fluid-injection protocol and extensive sensor array. *Geophys J Int* 208:790–813
- Zang A, Zimmermann G, Hofmann H, Stephansson O, Min KB, Kim KY (2019) How to reduce fluid-injection-induced seismicity. *Rock Mech Rock Eng* 52:475–493
- Zhang F, Damjanac B, Maxwell S (2019) Investigating hydraulic fracturing complexity in naturally fractured rock masses using fully coupled multiscale numerical modeling. *Rock Mech Rock Eng* 52:5137–5160
- Zhou Z, Zhang G, Dong H, Liu Z, Nie Y (2017) Creating a network of hydraulic fractures by cyclic pumping. *Int J Rock Mech Min Sci* 97:52–63
- Zhou C, Wan Z, Yuan Z, Gu B (2018) Experimental study on hydraulic fracturing of granite under thermal shock. *Geothermics* 71:146–155
- Zhuang L, Diaz MB, Jung SG, Kim KY (2016) Cleavage dependent indirect tensile strength of Pocheon granite based on experiments and DEM simulation. *Tunn Undergr Sp KSCE* 26(4):316–326

- Zhuang L, Kim KY, Jung SG, Diaz M, Min KB, Park S, Zang A, Stephansson O, Zimmermann G, Yoon JS (2018a) Cyclic hydraulic fracturing of cubic granite samples under triaxial stress state with acoustic emission, injectivity and fracture measurements. In: Proceedings of the 52nd US Rock Mechanics/Geomechanics Symposium, Seattle, ARMA 18–297
- Zhuang L, Kim KY, Yeom S, Jung SG, Diaz M (2018b) Preliminary laboratory study on initiation and propagation of hydraulic fractures in granite using X-ray Computed Tomography. In: Proceedings of International Conference on Geomechanics, Geo-energy and Geo-resources (IC3G2018), Chengdu, paper No. 151
- Zhuang L, Kim KY, Jung SG, Diaz M, Min KB (2019) Effect of water infiltration, injection rate and anisotropy on hydraulic fracturing behavior of granite. *Rock Mech Rock Eng* 52:575–589
- Zhuang L, Jung SG, Diaz M, Kim KY, Min KB, Zang A, Stephansson O, Zimmermann G, Yoon JS, Hofmann H (2019) Cyclic hydraulic fracturing of Pocheon granite cores and its impact on breakdown pressure, acoustic emission amplitudes and injectivity. *Int J Rock Mech Min Sci*. <https://doi.org/10.1016/j.ijrmm.2019.104065>
- Zhuang L, Kim KY, Diaz M, Yeom S (2020) Evaluation of water saturation effect on mechanical properties and hydraulic fracturing behavior of granite. *Int J Rock Mech Min Sci* <https://doi.org/10.1016/j.ijrmm.2020.104321>
- Zimmermann G, Tischner T, Legarth B, Huenges E (2009) Pressure-dependent production efficiency of an Enhanced Geothermal System (EGS): stimulation results and implications for hydraulic fracture treatments. *Pure Appl Geophys* 166:1089–1106
- Zimmermann G, Moeck I, Blöcher G (2010) Cyclic water-frac stimulation to develop an enhanced geothermal system (EGS)—conceptual design and experimental results. *Geothermics* 39(1):59–69
- Zimmermann G, Zang A, Stephansson O, Klee G, Semikova H (2019) Permeability enhancement and fracture development of hydraulic in situ experiments in the Åspö hard rock laboratory, Sweden. *Rock Mech Rock Eng* 52:495–515

Publisher's Note Springer Nature remains neutral with regard to jurisdictional claims in published maps and institutional affiliations.